Buckling Tests of Cylindrical Composite Shells in Multiaxial Loading

Stefan Panek *, Niklas Reuter†, Tobias S. Hartwich‡, Benedikt Kriegesmann§ and Dieter Krause¶
Hamburg University of Technology (TUHH), Hamburg, 21073, Germany

Thin-walled cylindrical composite shells are prone to buckling failure in a variety of load cases. The number of influencing factors and comparably small amount of test data on combined load cases, which regularly occur in application, pose a major design challenge. Two experimental campaigns on the buckling of thin-walled cylindrical composite shells in multiaxial loading are carried out with two nominally identical specimens with a radius-to-thickness-ratio of 375. The results of buckling tests with combined axial compression and torsion, compression and bending, as well as all three buckling critical load types are presented. The influence of the loading direction of bending and torsion is shown, and the effects of repeated mounting of the specimens in the test rig as well as the scatter of buckling loads are discussed. Comparison of test results with the established NASA SP-8007 guideline and perfect buckling loads shows major qualitative and quantitative differences in the load interaction curves.

Nomenclature

$\mathbf{P_{BL}}$	=	vector of experimental buckling load	kN, kNm, kNm
P_B	=	global bending moment at buckling,	kNm
P_C	=	axial compression force at buckling	kN
P_T	=	torsional moment at buckling	kNm
R	=	inside shell radius	mm
$\mathbf{S_{BL}}$	=	vector of buckling shell stresses	MPa
$\mathbf{S_{perf}}$	=	vector of buckling shell stresses for a perfect shell	MPa
t	=	shell wall-thickness	mm
κ_B	=	load ratio of compression-bending combination	degrees

Presented as Paper 2025-2335 at the AIAA 2025 SciTech Forum, Orlando, Florida, USA, 6-10 January 2025,

*Research Associate, Institute of Product Development and Mechanical Engineering Design (PKT), corresponding author, E-mail address: stefan.panek@tuhh.de
†Research Associate, Institute for Structural Mechanics in Lightweight Design (SML).
‡Research Associate, Institute of Product Development and Mechanical Engineering Design (PKT)
§Full Professor, Institute for Structural Mechanics in Lightweight Design (SML)
¶Full Professor, Institute of Product Development and Mechanical Engineering Design (PKT)

κ_T	=	load ratio of compression-torsion combination	degrees
λ_S	=	normalized load factor of buckling stresses	—
σ_b	=	shell stress component from bending load	MPa
σ_c	=	shell stress component from axial compression load	MPa
τ_t	=	shell shear stress component from torsion load	MPa

I. Introduction

In aerospace applications, thin-walled cylindrical shells are widely used as structural elements based on their high specific stiffness and load carrying capacity. Under certain critical load cases, particularly axial compression, bending, torsion, as well as combinations of those, sudden structural failure by buckling can occur in these shells. The buckling load of cylindrical shells is known to be influenced by numerous factors to varying degrees, such as geometric imperfections, imperfect load introduction, boundary conditions, and material properties [1, 2]. It has been shown in several studies that the use of lightweight design materials, e.g., carbon fiber reinforced plastics (CFRP) or other fiber composites, introduces a number of additional influencing factors, including the composition and stacking sequence of the laminate as well as the manufacturing process [3, 4].

A number of test campaigns have been conducted over the past decades, investigating the buckling of cylindrical composite shells in axial compression, with the available data base currently containing results from almost 240 tested shells, see e.g. [5–8]. Regarding multiaxial loading of CFRP shells with combinations of the aforementioned buckling critical load cases, despite being relevant to practice, much fewer experimental data are found in literature, most of which exclusively consider the combination of axial compression and torsion, e.g. [9–12]. The only experimental study to consider the buckling of cylindrical CFRP shells in bending, presented in [13], was conducted on a special test rig designed to apply pure bending but did not allow to introduce any other load types. Consequently, the most widely established deterministic design approach for cylindrical shells in combined loading presented in NASA guideline SP-8007 refers to the lack of empirical data as main cause to rely on potentially very conservative assumptions regarding the calculation of design loads [1].

The objective of this contribution is to analyze the buckling behavior and load interaction curves of cylindrical CFRP shells with high slenderness in multiaxial loading. For this purpose, two shells are investigated in experimental campaigns, in each of which repeated buckling tests under various different combinations of axial compression, torsion, and bending in different directions are conducted. The experimental results are presented and discussed, and the resulting load interaction curves are compared to the perfect buckling loads as well as the design loads given by NASA SP-8007.

II. Methodology

A. Test specimens

The two nominally identical CFRP shells considered in this contribution were manufactured at the German Aerospace Center (DLR) in Braunschweig in a semi-automatic hand lay-up process. This entailed the deposition and fixation of individual ¼" slit-tapes on the winding mandrel until each of the six layers was completed, as opposed to a classical filament winding process which would result in fiber undulations at the crossing points of the tapes. The pseudo quasi-isotropic laminate layup was chosen to allow for better comparability to the cylinders tested in [7]. The layup is only balanced instead of symmetric as in this fabrication process two layers with the same orientation cannot be laid on top of each other without the lower one being lifted or moved. The inner- and outermost layer have a slight deviation of 0.2° from the nominal specification due to being continuously wound along the entire length of the shells. Both cylinders have been previously tested in pure axial compression with no discernible damage or decrease in load carrying capacity or stiffness [14]. The nominal and measured specifications of the geometry and laminate for both shells are given in Table 1. Photogrammetric measurements of the shell surface were carried out prior to testing in order to record the geometric imperfection patterns. Detailed descriptions of the manufacturing process, the measured shell geometry, the test results of the past experiments, and the material properties of the used AS7/8552 Prepreg have been determined in [7] and [14] and are given in Table 2. The measured geometric imperfection data of both shells have been published in [15] in the well-established form of Fourier coefficients as described, e.g., in [16, 17].

Table 1 Nominal and measured properties of tested shells [14]

	Nominal	Z5LG	Z6LG
inside radius, mm	300.0	300.2	300.2
free length, mm	750	750	750
wall thickness, mm	0.80	0.84 ± 0.03	0.85 ± 0.03
laminate layup	$[90, -30, 30, -30, 30, 90]$	$[90.2, -30, 30, -30, 30, 90.2]$	
fiber/matrix system	AS7/8552 Prepreg, ¼" slit-tape		
manufacturing process	semi-automatic, layer-by-layer		

Table 2 Material properties of AS7/8552 Prepreg for nominal wall thickness, based on [7]

Nominal layer thickness	0.13 mm
Fiber Volume Fraction	57.42%
E_{11} (tension)	147,872 MPa
E_{11} (compression)	136,013 MPa
E_{22}	10,714 MPa
G_{12}	3,784 MPa
ν_{12}	0.32

In order to ensure a homogeneous load introduction and to allow for the application of bending and torsion load

in addition to axial compression, the shells were mounted in the clamping elements presented in [14]. Fig. 1 shows a schematic cross-section of one of these ring-like elements, consisting of a fitted inside ring that is centred on the base plate and an outside ring that leaves a small gap to the shell. This fixture covers 25 mm of the shell length at both ends and, with the epoxy potting, approximates fully clamped boundary conditions. The shell edges were still encased in the epoxy resin which was undamaged from previous tests and made it possible to efficiently re-use this potting. The clamping elements are designed such that the surface of the outside ring in contact with the epoxy potting is not smoothly circular but instead cut into a regular wave pattern, illustrated by the dashed line in Fig. 1, thus realizing positive locking in addition to load transfer by friction. This wave pattern has an amplitude of 2.5 mm and a period of 6°, resulting in 60 full waves along the entire circumference.

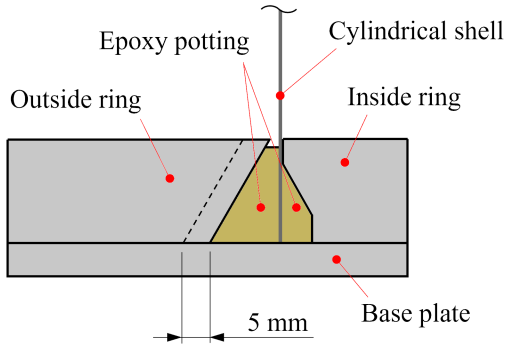

Fig. 1 Schematic cross-section of clamping element at the shell edge.

B. Test setup and procedure

Buckling tests are carried out at the Hexapod test rig at Hamburg University of Technology (TUHH), utilizing the same test setup as described in detail in [14]. This servo-hydraulic test rig allows for uniaxial and multiaxial static and dynamic testing by rotation and translation of the test platform in six degrees of freedom (DoF) [18]. Reaction forces and moments at the bottom edge of the shells are measured via a 6-DoF load cell, whereas displacements are tracked with the test rigs internal position sensors, as well as three optical sensors distributed along the circumference of the shells, pictured in Fig. 2. In addition, a photogrammetric system for digital image correlation (DIC) is employed, as in recent experimental studies [19, 20]. This way, it is possible to account for the stiffness of the test rig and test setup when analyzing the experimental results. Axial compression load is applied to the shells by lowering the test platform at a constant rate of 0.045 mm/s. Torsion and bending moments are introduced via rotation of the test rig about a point in the center of the shell located at half of the shell length at a rate of 0.01 °/s. This way, it is possible to minimize the position error, and thus the introduction of load imperfections, in load cases with a bending component.

In order to gather experimental data covering the majority of the load interaction curves, a set of 31 load combinations are selected for the first test campaign. These include tests with combined torsion and compression, compression and

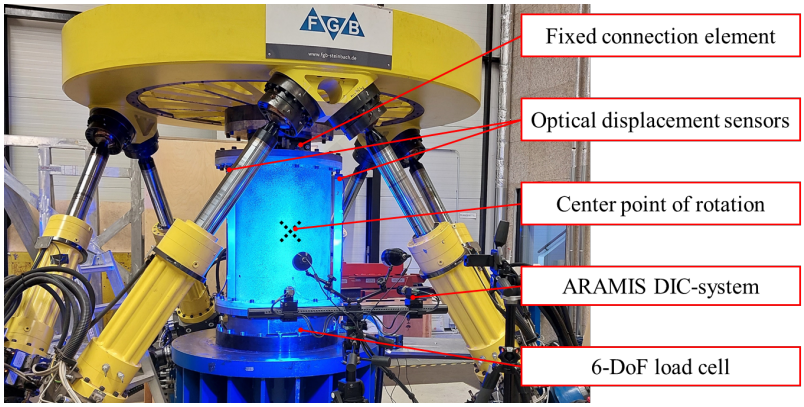

Fig. 2 Experimental setup at the Hexapod test rig.

bending, as well as different ratios of all three load types. The compression-bending tests are repeated with two different bending directions, thus providing data to investigate the influence of load direction. No tests with pure torsion or pure bending are carried out, as those have a higher chance to cause damage or degradation in the shell or the epoxy used in the clamping. As it has been shown in [12] that the loading sequence has no significant influence on the buckling load, the different load combinations are realized by first pre-loading the shells up to a predefined level with one or two of the investigated load types. Following this, the test rig is set to increase the desired loads at constant rates until buckling occurs, at which point the movement is stopped instantly and after a few seconds the load is reduced again until the shell is force-free. To ensure reproducible results, for each investigated load combination a minimum of five buckling tests is carried out.

A second study is conducted with both shells to gather additional data for load combinations and loading directions that were not investigated in the first one. In order to qualify uncertainties and influences of reattaching the specimens in the test rig for the second experimental campaign and thus checking for comparability between studies, several buckling tests with previously tested load combinations are repeated in the second test series. Throughout both test series, at certain intervals buckling tests with pure axial load are done to verify that no degradation occurred. A brief summary of all load ratios that were investigated across both test campaigns is given in the appendix of this work in Tables A1 - A4 by way of the mean buckling loads at each test point. A more detailed description of the individual load ratios and loading sequences can be found in [21].

C. Analysis and normalization of buckling loads

In multiaxial load cases, all three buckling critical load types need to be considered as components of the buckling load. Hence, one option is to define a buckling load vector $\mathbf{P_{BL}}$ comprised of axial compression force P_C, bending moment P_B and torsional moment P_T. However, due to the different underlying units, in some cases defining the buckling load as the maximum acting load may be challenging. Particularly in cases where no sudden failure occurs or

some load components gradually decrease before the onset of buckling, this may lead to biased results. Hence, in this study the moment in which buckling occurs is defined as the instant of maximum acting shell stresses, summarized in the stress vector $\mathbf{S_{BL}}$. The stress components σ_c, σ_b and τ_t that are caused by compression, bending and torsion respectively are calculated with the formulas in Eqs. (1) taken from EN 1993-1-6 [22].

$$\mathbf{S_{BL}} = \begin{bmatrix} \sigma_c \\ \sigma_b \\ \tau_t \end{bmatrix} \qquad \text{with} \qquad \sigma_c = \frac{P_c}{2\pi R t} \quad ; \quad \sigma_b = \frac{P_b}{\pi R^2 t} \quad ; \quad \tau_t = \frac{P_t}{2\pi R^2 t} \tag{1}$$

The design loads according to NASA SP-8007 as well as numerical perfect buckling loads are calculated for each load combination based on the nominal shell specification to contextualize the achieved experimental results. NASA design loads are determined using the analytical buckling load formulas provided in [1] for each buckling inducing load type separately. Interaction curves for the design load are then derived based on the assumption of linear load interactions between the three load components, as specified in the design guideline [1]. The buckling load interaction curves for the perfect shell are calculated as the first positive eigenvalue found for each load ratio by a linear buckling analyses (LBA) in ABAQUS. The numerical model utilized for these calculations is based on the one described in [14] and [23]. A mesh size of 3 mm is chosen for the S4R shell elements along both directions, based on a mesh convergence study carried out in [14]. Convergence studies were also conducted for torsion and bending loads to check whether convergence behavior changes with load type. Taking the results of a 1 mm mesh as a reference, it was found that a 3 mm mesh yields for all three load cases deviations of less than 0.5%. The nodes at both shell edges are rigidly tied to a central master node, representing the clamped boundary conditions. As in the experimental setup, bending loads are introduced by rotation about a central point at half of the shell height, which is rigidly coupled with the master node at the upper shell edge. Torsion load is applied by rotation of the upper master node about the cylinder axis. The master node at the bottom of the shell in turn has all its DoF blocked, thus representing the fixed connection to the load cell in the experimental setup.

The concept of a normalized load factor, as presented in [23], is adapted in this study to allow for comparison among results as well as to quantify how the discrepancies between design load, experimental result and perfect buckling load change with the load ratio. Whereas in [23], the load factor is calculated using the buckling load and bending moment, here the load factor λ_S is formulated according to Eq. (2) and represents the normalized projection of the buckling stress vector $\mathbf{S_{BL}}$ onto the vector of perfect buckling stresses $\mathbf{S_{perf}}$. Herein, $\mathbf{S_{BL}}$ can be taken as either an experimental result or the design load for the desired load ratio. The projected buckling stress can be determined by multiplication of λ_S with the perfect buckling stress $\mathbf{S_{perf}}$, which in turn can be converted into the projected buckling load as shown in

Eq. (3). This is achieved by inversion of the stress formulas given in Eq. (1). Thus, a direct comparison of magnitude and intuitive representation of buckling loads, for example in case of multiple test results that scatter somewhat in load ratio, is possible.

$$\lambda_S = \frac{\mathbf{S_{BL}} \cdot \mathbf{S_{perf}}}{\left\| \mathbf{S_{perf}} \right\|^2} \tag{2}$$

$$\mathbf{P_{projected}} = \lambda_S \cdot \pi R t \begin{bmatrix} 2\,\sigma_{c,perf} \\ R\,\sigma_{b,perf} \\ 2R\,\sigma_{t,perf} \end{bmatrix} \tag{3}$$

$$\kappa_B = \arcsin\left(\frac{\sigma_b}{\sqrt{\sigma_b^2 + \sigma_c^2}}\right) \quad \text{and} \quad \kappa_T = \arcsin\left(\frac{\tau_t}{\sqrt{\tau_t^2 + \sigma_c^2}}\right) \tag{4}$$

Additionally, a way to describe the investigated load ratios is introduced with κ_B and κ_T in Eq. (4). In this study, these normalized load ratios are defined as angles that measure the ratio of stresses induced by bending and torsion relative to the stress from axial compression. A schematic visualization of the angles representing the load ratios is shown in Fig. 3 for an exemplary test point $\mathbf{S_{BL}}$ that includes all three load components negative torsion, bending, and axial compression. In the pictured example, the resulting load ratios are $\kappa_B > 0°$ and $\kappa_T < 0°$, whereas buckling under a combination of only compression and positive torsion yields $\kappa_B = 0°$ and $\kappa_T > 0°$.

This normalization of load ratios is also applicable to the load components P_C, P_B and P_T instead of the buckling stresses. In that case, the aforementioned difference in units and hence in magnitude does lead to different values for the angles of load ratios. Furthermore, it is to note that due to the chosen reference for the load ratios, tests or calculations without axial load cannot be accurately represented. However, in this study all investigated load ratios include some axial compression load. Hence, this edge case is not considered further in this work.

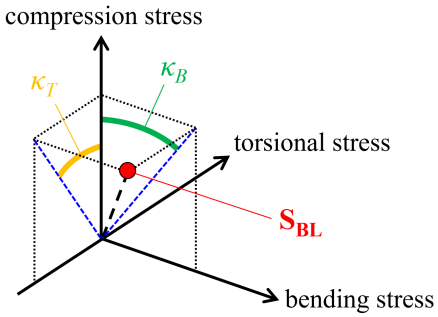

Fig. 3 Schematic depiction of the load ratios κ_B and κ_T.

III. Experimental Results

A. Buckling loads

In total, more than 300 buckling tests are carried out with each shell. A summary of the buckling loads achieved in all tests across both campaigns is visualized in Fig. 4 for the investigated shells. In both diagrams, the experimental buckling loads are compared to the design load envelope formed by the linear load interaction curves according to NASA SP-8007. The mean buckling loads for each test point are summarized in Tables A1 - A4 in the Appendix of this work. Detailed test results from all experiments, including the buckling load components P_C, P_B and P_T as well as the measured loading imperfections have been published with open access in [21].

The experimental studies were concluded without visually apparent degradation or damage to the test specimens. After disassembly of the clamping elements, no damage or significant degradation was found during visual inspection of the epoxy potting either. The repeated tests in axial compression over the course of both campaigns mostly showed relatively small changes in buckling load over time. Both shells exhibited a standard deviation of less than 0.8 kN in total across these repetitions. In initial tests, Z5LG achieved a buckling load in axial compression of 53.8 $\pm$ 0.2 kN and Z6LG buckled at 59.2 $\pm$ 0.2 kN, whereas in the experiments from [14], these specimens yielded mean buckling loads of 55.9 $\pm$ 0.2 kN and 58.9 $\pm$ 0.3 kN respectively. Shell Z5LG exhibited a slight increase in buckling load over the first campaign. After remounting for the second test series, the shell reached significantly higher buckling loads in axial compression with 57.8 $\pm$ 0.1 kN, again with a slight increase over the course of the experiments.

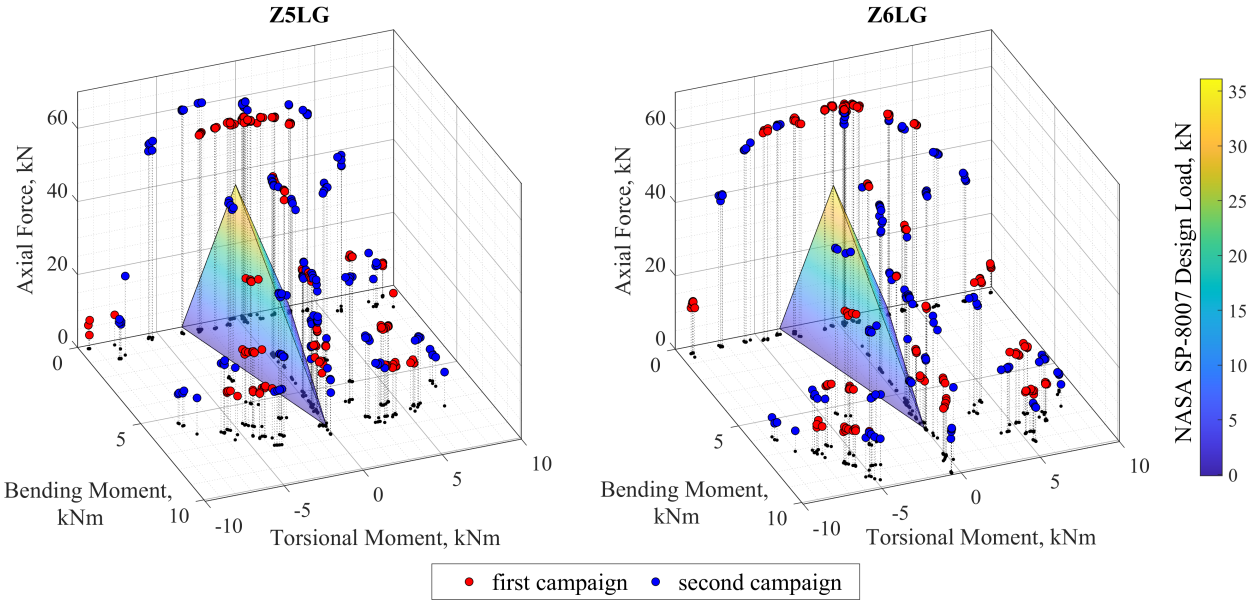

Fig. 4 Experimental buckling loads overlaid with NASA SP-8007 design load for the two tested specimens Z5LG (left) and Z6LG (right).

In contrast, for shell Z6LG during the first campaign a small steady decline in axial buckling load is observed,

whereas in the second test series the buckling load remained constant within the expected scatter and only decreased suddenly after about 130 buckling tests by approximately 2.4 kN. From this point until the end of the campaign however, the level of buckling loads remained constant. This drop in axial buckling load corresponds to a change in the buckling pattern, which is visualized by DIC measurements in Fig. 5. Similar to the findings in [14], shell Z6LG exhibits audible local pre-buckling during most tests with high axial compression loads, which is also visible in the load-displacement-curves for these tests, as shown exemplary in Fig. 6 for one experiment of the first test point in the second test series, supported by DIC measurements. The emergence of the local buckle is accompanied by a popping sound, immediately preceding the global failure of the shell.

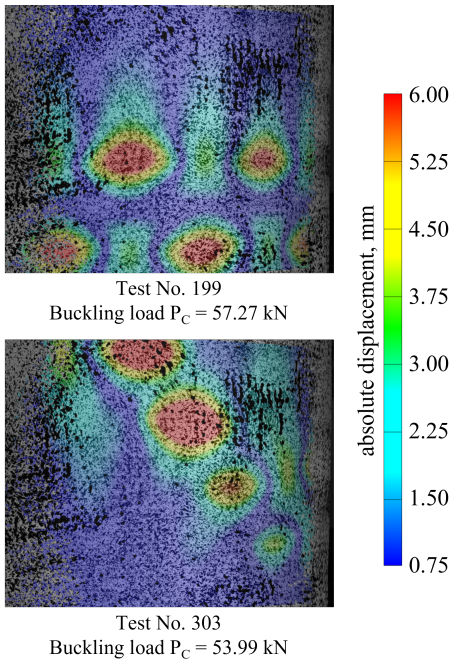

Fig. 5 DIC measurements showing change of buckling pattern in pure axial compression tests with Z6LG.

Axial shell stiffness values were determined from data recorded by the optical displacement sensors and remained constant within the expected scatter at 103.0 ± 1.3 kN/mm for Z5LG and 105.1 ± 1.5 kN/mm for Z6LG over the course of both campaigns. No significant change in axial stiffness was observed between the two test series. In contrast, it was noticed that in tests with larger torsion load some settling or sliding of the shells within the clamping elements occurred. When the loading direction was changed for tests with 8 kNm torsional pre-load, the test platform could be rotated by about 0.5° before a significant build up of torque began. In addition, both torsional and bending stiffness values appear to exhibit reproducible regressive behavior across both test series. In case of Z6LG for example, the mean bending stiffness in tests with large axial force and small bending moments amounts to 80.2 ± 1.4 kNm/° but for large bending loads the resulting stiffness drops to values between 65.4 kNm/° and 57.7 kNm/°, depending on the bending direction. This regressive stiffness behavior points towards the strength of the occurring Brazier forces being greater than other

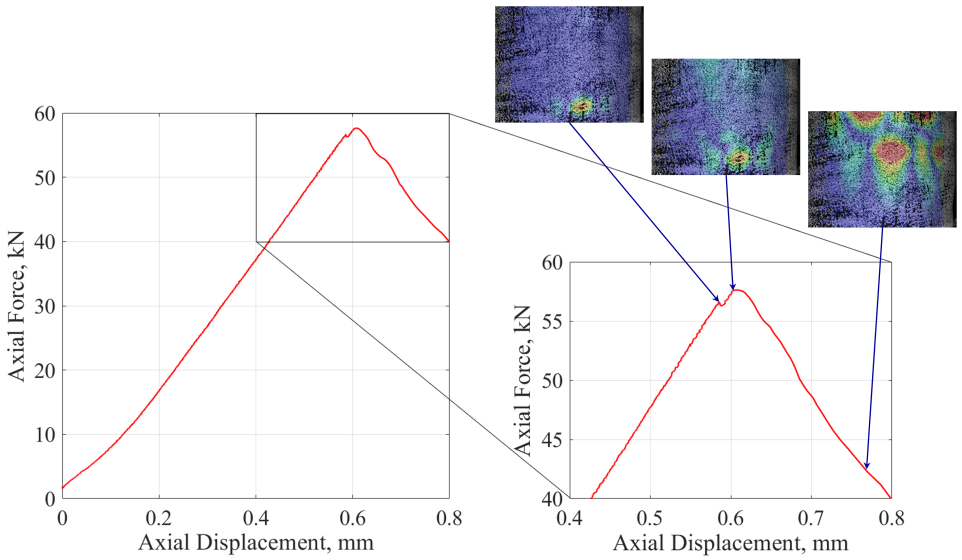

Fig. 6 Load displacement curve of axial compression buckling test with Z6LG and visible local buckling.

stabilizing effects.

In the left diagram of Fig. 4 it can be seen that for Z5LG significant changes in buckling load occur between the first study (in red) and the second one (in blue) not just in case of pure compression, but also for some combined load cases. In particular, tests with high axial force yield larger buckling loads in the second test series. On the other hand, no significant change in buckling loads between test campaigns with Z6LG is visible for these same load ratios. This is particularly apparent in Fig. 7 when considering the axial buckling loads corresponding to tests with about -2.5 kNm and 3.0 kNm torsional load.

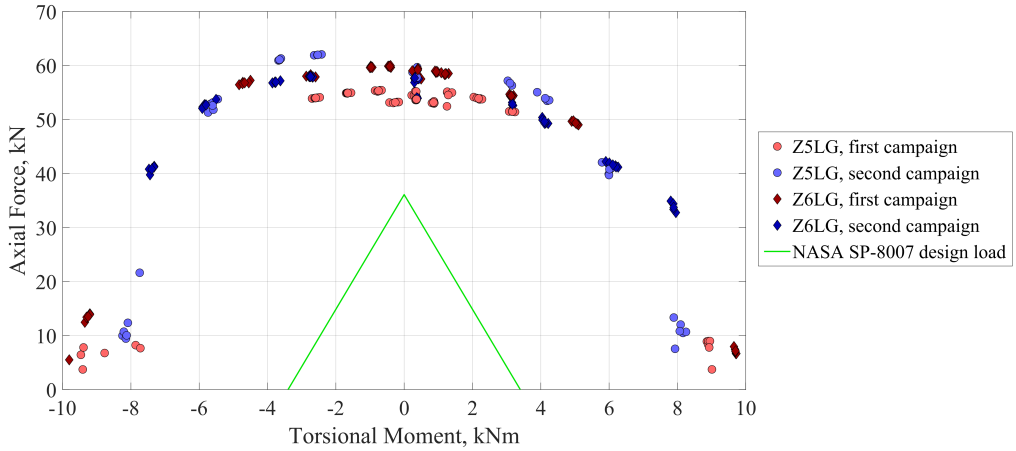

Fig. 7 Test results in compression-torsion compared with NASA SP-8007 design load.

Overall, the visualization of experimental buckling loads in Fig 7 of test points with compression-torsion combinations shows a consistent shape of the buckling load interaction curve across both shells and test campaigns. Similar to the experiments in [11] and [12], a strongly non-linear interaction between compression and torsion load is observed,

however the qualitative shape of the interaction curve differs somewhat from these previous studies. Furthermore it is apparent that the maximum of axial load carrying capacity is not found at pure axial compression, but rather in combination with negative torsion. Indeed, for shell Z5LG the maximum of axial buckling load at 62.1 kN is only achieved during the second test series in combination with -2.4 kNm torque. This amounts to an increase in buckling load by 4 % compared to pure axial compression tests. In case of Z6LG, no such pronounced increase in axial load is observed where the highest axial load is reached for -0.4 kNm torsion at 59.8 kN which is only 1 % larger than in pure compression tests. However, the introduction of torque loads up to about -2.7 kNm does not impose a reduction of axial load carrying capacity compared to pure compression loading, whereas positive torsion of 3.2 kNm leads to a decrease in axial buckling load by about 7.5 %. For test points with axial loads larger than 30 kN the scatter between individual tests appears to relate mostly to the achieved load ratios rather than to the magnitude of buckling loads. In contrast, the tests done with large torque in both positive and negative direction exhibit significantly stronger scatter.

Tests with combined compression-bending load were conducted in all four cardinal directions with respect to the coordinate system of the shells and the test rig, with the same sequence of axial pre-load in all directions. The buckling loads achieved in those experiments are presented in Fig. 8 with dashed lines indicating the estimated shape of load interaction curves based on the test data. In the first test campaign, positive bending was applied about the X-axis and negative bending about the Y-axis, resulting in nominal bending directions of 270° and 180° respectively. Consequently, tests in the second series were done with negative bending about the X-axis and positive bending about the Y-axis. Due to the differences in axial buckling load measured after remounting the specimens for the second campaign, sample tests are done with the same bending directions as in the first series. The results of these experiments are shown for both shells in Fig. 8 as well, represented in light blue without an indication of the interaction curve. Shell Z5LG exhibits qualitatively and quantitatively similar load interaction curves for all four bending directions. The aforementioned repetition of test points from the first campaign yields on average 0.5 kNm larger bending moments in experiments with axial pre-loads of 30 kN and 45 kN. Generally, for Z5LG it can be seen that bending about the Y-axis, that is towards 180° and 0°, causes buckling at lower loads than bending about the X-axis.

The largest difference is found for the repetition tests in the second campaign with 15 kN axial pre-load and amounts to about 1.9 kNm which corresponds to 24 % of the maximum bending moment recorded. In the left diagram of Fig. 8 it can also be seen that during the first test campaign, global buckling occurred in tests with the largest ratio of bending to compression at slightly lower moments than in tests with higher axial pre-load. After remounting the shell for the second campaign, repetition of these four test points does yield slightly higher moments in 270°-direction whereas the resistance to bending in 180°-direction is slightly lower for all load ratios.

On the other hand, for Z6LG positive bending about the X-axis, i.e. in 270°-direction, results in the highest buckling loads with average bending moments for all load ratios at least 1.4 kNm larger than for the remaining bending directions. The lowest bending loads are achieved in 180°-direction, with the sample tests in the second experimental study yielding

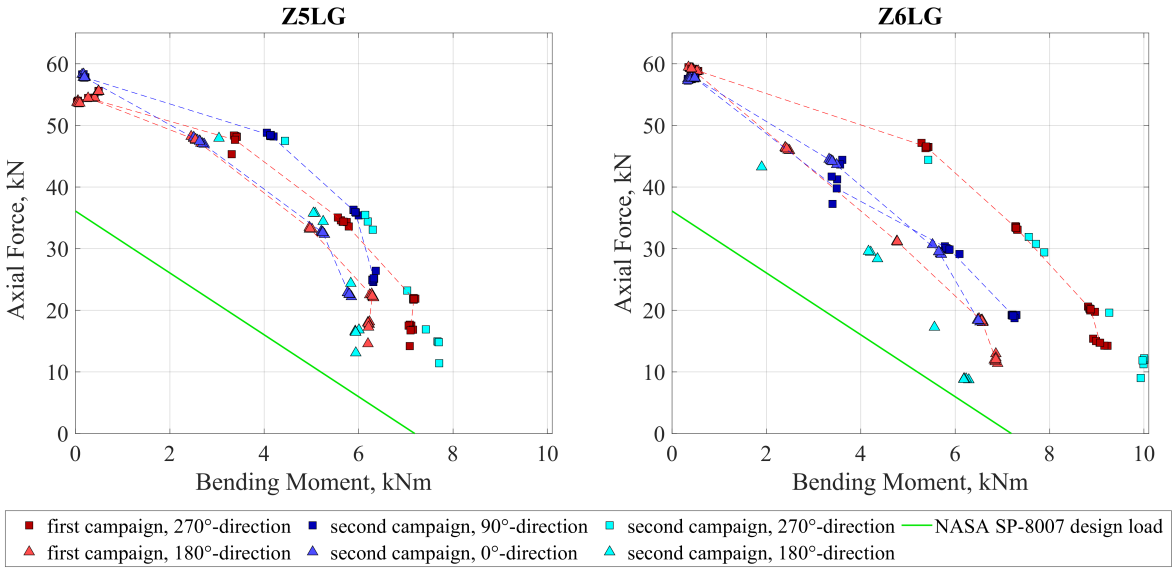

Fig. 8 Test results in compression-bending compared with NASA SP-8007 design load.

even lower values than in the first one. The absolute span between highest and lowest bending load varies from 3.3 kNm to 3.8 kNm and thus remains nearly constant for all load ratios. Generally, the load interaction curves of Z5LG appear to follow a curve similar to the one emerging from compression-torsion combination, for Z6LG the behavior is closer to a linear interaction for the individual bending directions. In turn, the directional differences in buckling load are significantly larger due to one particular bending direction yielding at least 23 % higher loads than all other cases.

B. Loading imperfections

In the context of this work, all deviations from the desired load ratio are considered as loading imperfections. This includes the occurrence or build up of undesired bending and torsion loads, as well as lateral shear forces acting on the shells during tests, particularly in the pre-buckling range immediately before the onset of buckling. During testing, all of these are recorded via the test rigs 6-DoF load cell.

Throughout both test series, in experiments with buckling induced by axial compression it is observed that the gradual increase of axial force causes a linear build-up of positive torque up to a certain level. This effect is especially apparent in tests with only compression-torsion combinations. During experiments with pure axial compression, at buckling a mean torque of 370 Nm is measured. This effect causes a shift in the achieved load ratios towards positive torsion which is notable in particular for those data points shown in Fig. 7 with small magnitudes of torque. On average, in both shells this occurs at a rate of 6.7 Nm per 1 kN of axial force. However, in tests where a torsional pre-load of more than 4 kNm in positive direction is applied, no further increase of torque is seen during axial loading. In contrast, for large negative torsion pre-loads this effect does persist. Just as the asymmetry of buckling loads with respect to the torque direction seen in Fig. 7, this effect is likely caused by the antisymmetric laminate layup. The relation between

axial force and shear load, which here can be converted into a torsional moment, in the elastic range is elaborated in [24]. The positive B_{16} coupling that is present in the layup induces a direct correlation, thus causing the general shift towards positive torsion.

The measured lateral forces acting on the shells are in the same range as in [14] for tests with pure axial compression, amounting to less than 0.8 kN across all tests. During compression-torsion experiments in the first test series, the lateral load imperfections remain consistent in magnitude and scatter. However, in the second campaign it is observed that for larger ratios of torsion, the lateral forces increase up to a maximum of 2.5 kN for shell Z5LG. Whereas for Z6LG the behavior is qualitatively similar, the magnitude of lateral forces remains below 1.2 kN. In contrast, the results of tests with combined compression-bending show for both studies that on average an increase in bending load is accompanied by a proportional increase in lateral force which is exemplified in Fig. 9 for one test with Z6LG. Although in this case the correlation between bending moment and magnitude of shear force is particularly apparent, the rate at which lateral forces increase varies with the direction that bending is applied in.

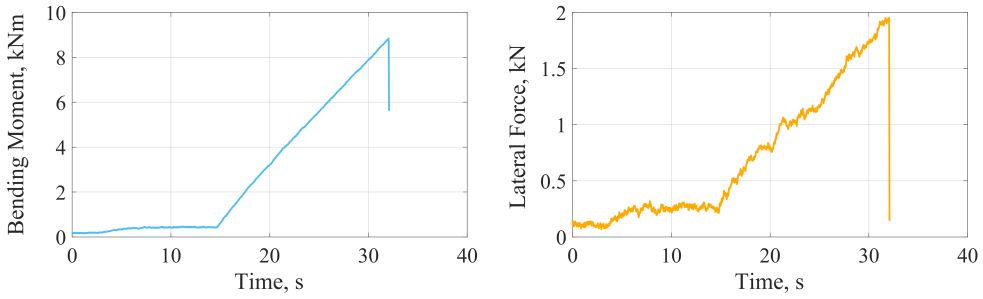

Fig. 9 Bending load and lateral force in a compression-bending test with Z6LG.

The largest lateral loads are recorded for test points which include large ratios of positive bending about the X-axis. During these tests, shear loads of up to 3.4 kN and 2.0 kN are measured for Z5LG and Z6LG, respectively. The acting direction of lateral forces often differs from the direction of bending loads by up to 40° for both shells in the first test series, whereas in the results of the second campaign a slightly closer alignment between the direction of bending and lateral force is observed. Furthermore, experiments with all three buckling inducing load types show that a change in the direction of torsion load can shift the vector of lateral forces by up to 60°.

IV. Analysis and Discussion

An initial comparison between the design load surface according to NASA SP-8007 and the experimental buckling loads, as visualized in Fig. 4, already shows that the linear load interaction curves of the deterministic design approach do not correspond well to the experimentally found load interactions for both shells. Particularly in cases that include moderate to large amounts of torsion, the design load is drastically lower than the test results. This is even more apparent in Fig. 7 where only tests with combined compression-torsion are considered. Similarly, the compression-bending

interaction observed in tests, as presented in Fig. 8, differs significantly from the one defined in the design guideline. Although the design loads are conservative with respect to all experimental results, the indicated shape of the interaction curves particularly for Z5LG leads to hypothesize that if pure bending loads were applied, the design may be not conservative for some bending directions.

In order to allow for better comparability between the different considered load ratios, the normalization of buckling loads and load ratios as introduced in Eqs. (2) and (4) is applied to all test data as well as the NASA design loads of the corresponding load ratios. This results in the representation shown in Fig. 10 for compression-torsion and Fig. 11 for compression-bending interaction which directly correspond to Figs. 7 and 8, respectively. Here, in all diagrams a value of $\lambda_S = 1$ equates to the first perfect buckling load found for the corresponding load ratio κ. In Fig. 10 it is noticeable that one test with Z6LG yields a result higher than the calculated perfect load. This is likely caused by a combination of a low imperfection sensitivity at this load ratio and the buckling mode occurring in the experiment not corresponding to the first eigenvalue, which was taken to be the perfect buckling load for this study.

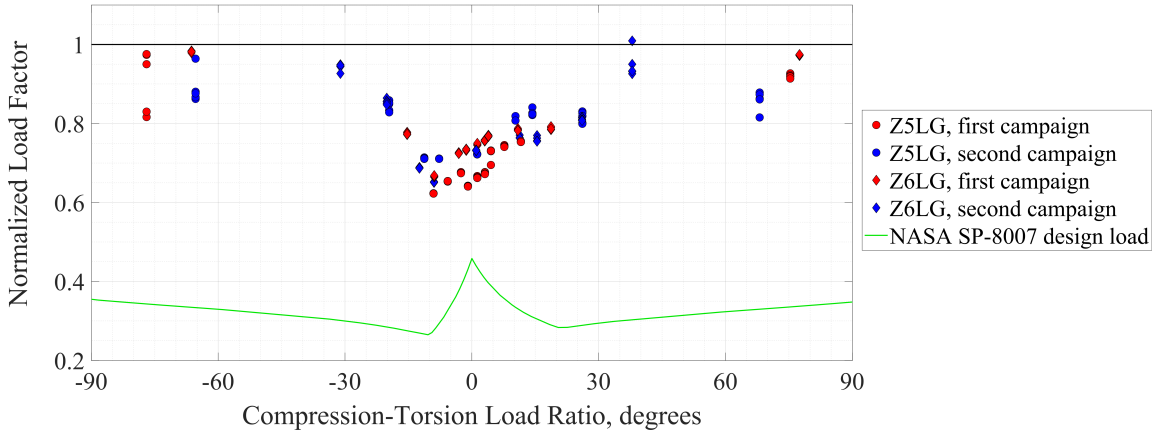

Fig. 10 Normalized buckling loads for compression-torsion tests.

With respect to the perfect buckling load, in compression-torsion tests as visualized in Fig. 10 the maximum discrepancy is seen for values of κ_T between 0° and -15° with normalized loads ranging from 0.62 to 0.73, even though these load ratios yield the highest absolute buckling loads. In contrast, for large positive and negative torsion ratios the discrepancy between perfect and experimental buckling load is less than 20 % whereas the scatter of load factors is broader for most tests, e.g. with values ranging from 0.82 to 0.98 at about -75°. Due to the distribution of test points, the range of torsion ratios from -30° up to 30° in particular clearly shows the gradual change of the difference between perfect load and test results. In addition, this visualization allows for a quantitative comparison of the NASA SP-8007 knockdown-factor to the experiments. For the isolated load cases of axial compression, bending, and torsion the design loads and the load factor with respect to the perfect load are summarized in Table 3. Normalization of the design load for all load ratios yields the green curve shown in Fig. 10. The closest fit to experimental buckling loads is seen at

pure compression load with a difference of 0.18 in load magnitude. Towards larger torsion ratios the conservative assumptions of the design guideline cause the discrepancy to grow up to 0.48 which corresponds to a safety factor of about 2.0 with respect to the experimental buckling load.

Table 3 Comparison of NASA SP-8007 design loads and perfect buckling loads

Load component	Design load	Perfect buckling load	λ_S
P_C	36.10 kN	78.79 kN	0.458
P_B	7.19 kNm	12.16 kNm	0.591
$P_{T,pos}$	3.40 kNm	9.77 kNm	0.348
$P_{T,neg}$	-3.40 kNm	-9.59 kNm	0.355

The depiction of load factors for compression-bending interaction in Fig. 11 shows some variation of the discrepancy between perfect load and test results over the load ratio κ_B as well as between the two shells. Whereas for Z5LG a maximum load factor of 0.91 is reached at a bending ratio of about 30° with a continuous decrease for larger load ratio angles down to 0.75 at 70°, in case of Z6LG positive bending about the X-axis yields load factors greater than 0.92 up to the same bending ratio. Furthermore, considering the lowest buckling loads achieved in experiments, a nearly constant lower boundary of the discrepancy can be seen for Z6LG with most tests yielding load factors of 0.7 or higher. For Z5LG the scatter of normalized loads appears to remain approximately constant for bending ratios greater than 25° with a total span of about 0.10, contrasted by the larger spread found for Z6LG which slightly decreases from a maximum span of about 0.28 to 0.21 with growing bending ratios. The normalization of design loads according to NASA SP-8007 for this load combination shows slightly better agreement with the perfect and experimental load interactions in comparison to compression-torsion interaction, with a nearly linear increase of load factors from about 0.46 to 0.59.

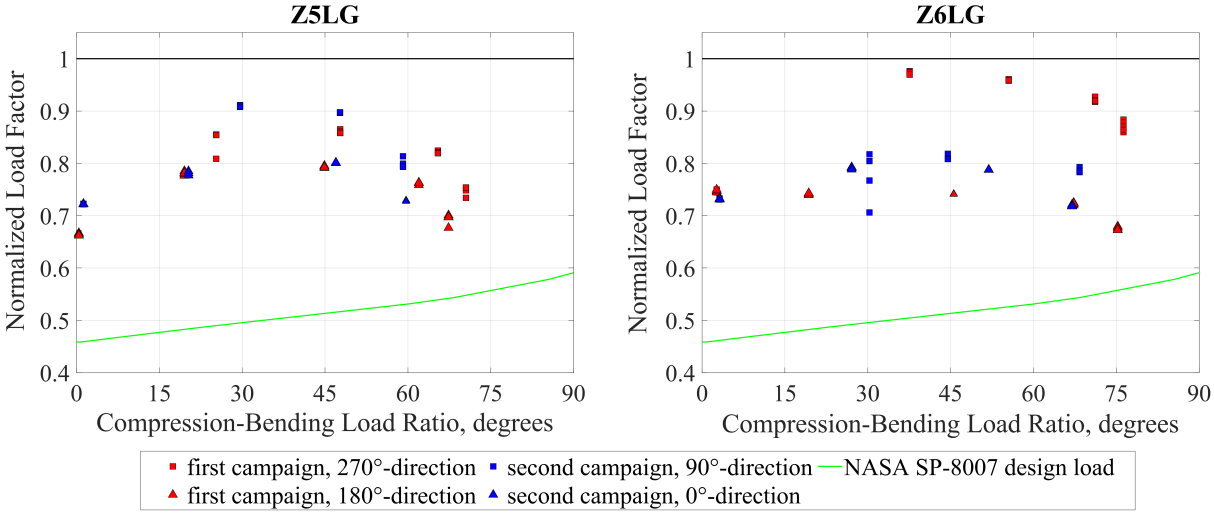

Fig. 11 Normalized buckling loads for compression-bending tests.

Generally, the difference between design load and experimental data is lower for this load combination than for

combined compression-torsion. However, the overall scatter of all test results is larger and in total less consistent than the one seen in Fig. 10. It is widely known that shells with a high R/t-ratio are generally more sensitive towards different kinds of influencing factors, which likely contributes to the high directional scatter seen for Z6LG in particular. A high sensitivity, e.g. towards loading imperfections such as the recorded lateral forces or possible eccentricities in the test setup and load introduction may also add to the larger scatter seen for high torsion load ratios between both shells as well as the non-linear load interactions observed for compression-bending in Z5LG. Furthermore, the changes in buckling load measured after repeated mounting of the shells in the test rig indicate the importance of not only the test rig boundary conditions, but also the process of assembling the test setup.

The observations for both interaction types confirm a general change in imperfection sensitivity for different load ratios as mentioned e.g. in [2] for geometric imperfections. In addition, the test data and the resulting discrepancy to the perfect load also point towards a shift in the influence of different factors that may cause the variation in scatter of test results.

V. Conclusion

A large number of buckling experiments was conducted on two nominally identical thin-walled cylindrical CFRP shells under various different combinations of the buckling critical load cases axial compression, bending, and torsion. In addition to the load ratios, the direction of applied torsion and bending loads was systematically varied. It is shown that the testing procedure yields reproducible results with comparably low scatter for most load ratios without inducing any significant damage or degradation in the test specimens. In addition, the changes in buckling load due to repeated mounting in the test rig are of similar magnitude as those caused by other common influence factors. The experimental results show strongly non-linear and direction-dependent load interaction curves for combined compression-torsion loading. In compression-bending tests, variation of the bending direction is found to cause differences of up to 20 % in the buckling load, thus ranking in the same magnitude of influences such as geometric imperfections.

Comparison of test data with the design loads given by NASA SP-8007 shows large discrepancies in the shape of load interaction curves and the predicted magnitude of buckling loads. It is observed that the discrepancy between perfect and experimental buckling load varies significantly across the considered load ratios, with some test results even exceeding the perfect load predictions. Furthermore, it is demonstrated that projection and normalization of test data in combination with the proposed description of load ratios allows for efficient and intuitive comparison of results between different load ratios. In addition, this representation of buckling loads offers an easy way to analyze the scatter of experimental data.

Although the experimental results presented in this work provide some valuable insight on the buckling behavior of cylindrical composite shells in combined load cases, the gathered amount of data is not sufficient to permit the use as a base for probabilistic analyses. Thus, additional test campaigns with comparable shells are necessary to provide

a well-founded data base. Furthermore, the interaction of different influence factors such as geometric and loading imperfections, the laminate layup, and the boundary conditions for different load ratios should be investigated in order to gain the understanding necessary for more reliable and robust buckling load predictions for combined load cases.

Appendix

The following tables summarize the mean values of the experimental buckling loads achieved across both test campaigns. A detailed list including descriptions of the specific loading sequence, individual test results and loading imperfections can be found in [21]. The test points are numbered according to the designation in [21], representing the chronological order of the tests. Data corresponding to load ratios that were repeated over the campaigns to check for reproducibility or degradation are left out in this overview.

Table A1 Mean buckling loads of Z5LG in first test series

Test point	P_C, kN	P_B, kNm	P_T, kNm	Test point	P_C, kN	P_B, kNm	P_T, kNm
1	53.75	0.06	0.36	**19**	33.77	5.08	-3.07
2	53.16	0.09	0.86	**20**	21.02	6.62	4.03
3	53.18	0.10	-0.26	**21**	20.47	6.41	-3.91
4	54.54	0.35	1.29	**22**	13.56	7.32	4.20
5	55.33	0.39	-0.75	**23**	12.30	7.02	-4.34
6	53.90	0.30	2.18	**24**	14.10	7.30	3.59
7	54.91	0.45	-1.65	**25**	13.46	7.12	-3.79
8	51.48	0.34	3.17	**26**	12.00	7.02	5.60
9	54.00	0.43	-2.59	**27**	10.52	6.39	-5.46
11	47.66	3.38	0.38	**28**	20.75	6.53	4.33
12	47.69	2.54	0.39	**29**	19.94	6.22	-4.35
13	34.38	5.68	0.17	**31**	7.80	0.64	8.93
14	33.25	4.97	0.25	**32**	6.77	0.29	-8.77
15	21.84	7.17	-0.04	**33**	16.74	7.10	-0.28
16	22.30	6.29	0.12	**34**	17.26	6.21	0.06
18	34.17	4.94	3.35				

Table A2 Mean buckling loads of Z5LG in second test series

Test point	P_C, kN	P_B, kNm	P_T, kNm	Test point	P_C, kN	P_B, kNm	P_T, kNm
1	57.80	0.19	0.38	**19**	33.77	6.24	-2.11
2	56.74	0.34	3.10	**20**	21.55	7.12	2.64
3	61.97	0.33	-2.53	**21**	21.92	7.23	-2.84
4	53.94	0.44	4.13	**22**	15.77	7.55	3.06
5	61.08	0.35	-3.65	**23**	14.94	7.73	-3.50
6	40.80	0.79	6.01	**24**	47.51	3.56	2.80
7	52.59	0.28	-5.61	**25**	47.58	3.48	-3.09
9	34.32	6.21	0.16	**26**	8.19	6.22	7.64
10	35.30	5.12	0.26	**27**	8.95	5.64	-7.76
11	48.41	4.13	0.26	**28**	18.58	7.08	5.87
12	47.42	2.63	0.24	**29**	19.18	6.53	-5.84
13	35.94	5.93	0.11	**31**	10.82	0.88	8.07
14	32.60	5.24	0.06	**32**	12.36	1.07	-8.09
15	25.19	6.32	0.13	**33**	14.58	7.64	-0.14
16	22.61	5.80	0.16	**34**	15.88	5.95	0.03
18	33.54	6.01	2.38				

Table A3 Mean buckling loads of Z6LG in first test series

Test point	P_C, kN	P_B, kNm	P_T, kNm	Test point	P_C, kN	P_B, kNm	P_T, kNm
1	59.21	0.41	0.40	**19**	31.88	6.49	-4.16
2	58.83	0.38	0.94	**20**	18.84	7.91	5.21
3	59.81	0.44	-0.42	**21**	17.85	7.81	-5.18
4	58.48	0.48	1.20	**22**	10.87	8.58	5.75
5	59.70	0.53	-0.97	**23**	9.20	8.28	-5.85
6	54.39	0.43	3.14	**24**	11.33	8.58	5.35
7	58.02	0.51	-2.73	**25**	9.96	8.60	-5.35
8	49.35	0.22	5.02	**26**	9.99	8.08	6.96
9	56.80	0.45	-4.67	**27**	7.44	7.30	-6.79
11	46.57	5.38	0.26	**28**	18.27	7.50	6.18
12	46.20	2.43	0.24	**29**	16.53	7.10	-6.04
13	33.36	7.29	0.04	**31**	7.16	0.31	9.70
14	31.16	4.77	0.17	**32**	13.51	0.41	-9.25
15	20.17	8.87	-0.13	**33**	14.73	9.07	-0.19
16	18.30	6.56	-0.02	**34**	12.03	6.86	0.12
18	33.02	6.34	4.16				

Table A4 Mean buckling loads of Z6LG in second test series

Test point	P_C, kN	P_B, kNm	P_T, kNm	Test point	P_C, kN	P_B, kNm	P_T, kNm
1	57.70	0.48	0.31	**19**	30.94	7.48	-3.60
2	52.82	0.42	3.17	**20**	17.33	8.30	4.31
3	57.95	0.33	-2.74	**21**	18.75	8.71	-4.39
4	49.64	0.33	4.11	**22**	9.49	9.11	5.43
5	56.93	0.31	-3.76	**23**	11.32	9.39	-5.06
6	41.60	0.47	6.11	**24**	44.60	3.24	3.29
7	52.70	0.35	-5.80	**25**	44.70	5.49	-3.92
9	30.69	7.72	0.22	**26**	5.19	6.81	8.82
10	29.12	4.24	0.20	**27**	4.93	6.33	-8.52
11	39.78	3.49	0.22	**28**	14.96	7.69	7.09
12	44.17	3.39	0.24	**29**	15.75	7.41	-6.99
13	39.87	5.88	0.13	**31**	33.73	0.52	7.89
14	29.51	5.65	0.07	**32**	40.81	0.34	-7.39
15	19.12	7.23	0.03	**33**	11.26	9.98	-0.53
16	18.37	6.49	0.02	**34**	8.82	6.22	-0.13
18	30.47	6.86	3.42				

Funding Sources

The research presented in this contribution was funded by the German Research Foundation (DFG) via the project "Experimental investigation and probabilistic analysis of the buckling load of cylindrical shells subjected to multiaxial load cases" (Project No. 463883313). The Hexapod test rig was funded by the DFG as well.

References

[1] Hilburger, M. W., "Buckling of Thin-Walled Circular Cylinders", NASA-SP-8007-2020/REV 2, NASA Langley Research Center, Hampton, Virginia, USA, 2020.

[2] Singer, J., Arbocz, J., and Weller, T., *Buckling Experiments: Experimental Methods in Buckling of Thin-Walled Structures: Shells, Built-Up Structures, Composites and Additional Topics*, John Wiley & Sons Inc, Hoboken, New Jersey, USA, 2002, Chaps. 9-11. https://doi.org/10.1002/9780470172995.

[3] Geier, B., Meyer-Piening, H., and Zimmermann, R., "On the influence of laminate stacking on buckling of composite cylindrical shells subjected to axial compression", *Composite Structures*, Vol. 55, 2002, pp. 467–474. https://doi.org/10.1016/S0263-8223(01)00175-1.

[4] Pai, S. P., and Jensen, D. W., "Influence of Fiber Undulations on Buckling of Thin Filament-Wound Cylinders in Axial Compression", *Journal of Aerospace Engineering*, Vol. 14, No. 1, 2001, pp. 12-20. https://doi.org/10.1061/(ASCE)0893-1321(2001)14:1(12).

[5] Takano, A., "Statistical Knockdown Factors of Buckling Anisotropic Cylinders Under Axial Compression", *Journal of Applied Mechanics*, Vol. 79, No. 5, 2012. https://doi.org/10.1115/1.4006450.

[6] Wagner, H., Hühne, C., and Elishakoff, I., "Probabilistic and deterministic lower-bound design benchmarks for cylindrical shells under axial compression", *Thin-Walled Structures*, Vol. 146, 2020, p. 106451. https://doi.org/10.1016/j.tws.2019.106451.

[7] Hartwich, T. S., and Panek, S., "Database of Static Buckling Experiments with Cylindrical Composite Shells under Axial Compression", Zenodo, 2023. https://doi.org/10.5281/ZENODO.7843039.

[8] Panek, S., Hartwich, T. S., Kriegesmann, B., and Krause, D., "Guidelines for test conditions and documentation of buckling experiments with cylindrical CFRP shells", *23rd International Conference on Composite Materials (ICCM23)*, 2023.

[9] Wilkins, D. J., and Love, T. S., "Combined Compression-Torsion Buckling Tests of Laminated Composite Cylindrical Shells", *Journal of Aircraft*, Vol. 12, No. 11, 1975, pp. 885–889. https://doi.org/10.2514/3.59889.

[10] Herakovich, C. T., "Theoretical-experimental correlation for buckling of composite cylinders under combined compression and torsion", NASA-CR-157358, Virginia Polytechnic Inst. and State Univ., Blacksburg, Virginia, USA, 1978.

[11] Meyer-Piening, H.-R., Farshad, M., Geier, B., and Zimmermann, R., "Buckling loads of CFRP composite cylinders under combined axial and torsion loading - experiments and computations", *Composite Structures*, Vol. 53, No. 4, 2001, pp. 427–435. https://doi.org/10.1016/S0263-8223(01)00053-8.

[12] Bisagni, C., and Cordisco, P., "An experimental investigation into the buckling and post-buckling of CFRP shells under combined axial and torsion loading", *Composite Structures*, Vol. 60, No. 4, 2003, pp. 391–402. https://doi.org/10.1016/S0263-8223(03)00024-2.

[13] Fuchs, H., Starnes, J., Jr, and Hyer, M., "Collapse of composite cylinders in bending", *38th Structures, Structural Dynamics, and Materials Conference*, 1997, p. 1241. https://doi.org/10.2514/6.1997-1241.

[14] Hartwich, T. S., Panek, S., Wilckens, D., Wille, T., and Krause, D., "The influence of R/t-ratio on the imperfection sensitivity of the buckling load of thin-walled CFRP cylindrical shells", *Composite Structures*, Vol. 341, 2024, p. 118216. https://doi.org/10.1016/j.compstruct.2024.118216.

[15] Hartwich, T. S., Panek, S., and Krause, D., "Geometric Imperfection Data of 7 thin-walled cylindrical shells with R/t-Ratio of 375", TORE, 2024. https://doi.org/10.15480/882.9613.

[16] Arbocz, J., and Abramovich, H., "The initial imperfection data bank at the Delft University of Technology: Part I", Report LR-290, Delft University of Technology, Department of Aerospace Engineering, 1979.

[17] Kriegesmann, B., Rolfes, R., Hühne, C., and Kling, A., "Fast probabilistic design procedure for axially compressed composite cylinders", *Composite Structures*, Vol. 93, 2011, pp. 3140–3149. https://doi.org/10.1016/j.compstruct.2011.06.017.

[18] Plaumann, B., Rasmussen, O., and Krause, D., "System analysis and synthesis for the dimensioning of variant lightweight cabin interior", *54th AIAA/ASME/ASCE/AHS/ASC Structures, Structural Dynamics, and Materials Conference*, 2013. https://doi.org/10.2514/6.2013-1632.

[19] Xin, R., Le, V. T., and Goo, N. S., "Buckling identification in composite cylindrical shells with measured imperfections using a Multi-DIC method and finite element analysis", *Thin-Walled Structures*, Vol. 177, 2022, p. 109436. https://doi.org/10.1016/j.tws.2022.109436.

[20] Rudd, M. T., Eberlein, D. J., Waters, W. A., Gardner, N. W., Schultz, M. R., and Bisagni, C., "Analysis and validation of a scaled, launch-vehicle-like composite cylinder under axial compression", *Composite Structures*, Vol. 304, 2023, p. 116393. https://doi.org/10.1016/j.compstruct.2022.116393.

[21] Panek, S., Hartwich, T. S., and Krause, D., "Test results from multiaxial buckling experiments on cylindrical CFRP shells with R/t-ratio of 375", TORE, 2024. https://doi.org/10.15480/882.14258.

[22] "Eurocode 3 - Design of steel structures - Part 1-6: Strength and Stability of Shell Structures", EN 1993-1-6, European Committee for Standardization, Brussels, Belgium, 2007.

[23] Reuter, N., Panek, S., Kriegesmann, B., Balokas, G., Hartwich, T. S., and Krause, D., "Experimental investigation and probabilistic analysis of the buckling load of isotropic cylinders under multiaxial loading", *Thin-Walled Structures*, Vol. 205, 2024, p. 112379. https://doi.org/10.1016/j.tws.2024.112379.

[24] Wong, K. F. W. and Weaver, P. M., "Approximate solution for the compression buckling of fully-anisotropic cylindrical shells", *AIAA journal*, Vol. 43, 2005, pp. 2639-2645. https://doi.org/10.2514/1.10924.